Journal of
Materials Chemistry A

COMMUNICATION

View Article Online
View Journal | View Issue

Cite this: *J. Mater. Chem. A*, 2016, **4**, 12025

Received 14th June 2016
Accepted 12th July 2016

DOI: 10.1039/c6ta05817e

www.rsc.org/MaterialsA

Exploring the properties of lead-free hybrid double perovskites using a combined computational-experimental approach†

Zeyu Deng, Fengxia Wei, Shijing Sun, Gregor Kieslich, Anthony K. Cheetham* and Paul D. Bristowe*

Density functional theory screening of the hybrid double perovskites $(MA)_2B^IBiX_6$ (B^I = K, Cu, Ag, Tl; X = Cl, Br, I) shows that systems with band gaps similar to those of the $MAPbX_3$ lead compounds can be expected for B^I = Cu, Ag, Tl. Motivated by these findings, $(MA)_2TlBiBr_6$, isoelectronic with $MAPbBr_3$, was synthesised and found to have a band gap of ~2.0 eV.

The remarkable performance of hybrid perovskite-based solar cells has launched a new paradigm in the area of photovoltaic research.[1] Facilitated by the processing flexibility of hybrid lead halide perovskites, *e.g.* $[CH_3NH_3]PbI_3$ and $[(NH_2)_2CH]PbI_3$, the turn-over efficiencies have soared to over 20% within a short period of time.[2–4] In materials such as $[CH_3NH_3]PbI_3$, which is the most widely studied phase, a 3D inorganic framework of the ReO_3-type is formed by $[PbI_3]^-$, whilst the $[CH_3NH_3]^+$ cation fills the dodecahedral void to form a perovskite-like structure. However, the inorganic $[PbX_3]^-$ framework with X = Cl^-, Br^- and I^- exhibits a highly dynamic character which is apparent in the thermal ellipsoids of the halide anions obtained from single crystal X-ray diffraction.[5,6] Together with the motion of the protonated cation, these materials exhibit disorder that poses challenges to crystallographers and computational scientists alike. For instance, expensive molecular dynamics (MD) simulations are usually required to access the electronic structures of the cubic and tetragonal polymorphs of $[CH_3NH_3]PbI_3$.[7,8] The exceptional performance of hybrid perovskites as light absorbing materials is attributed to the nearly perfect intrinsic properties, such as tuneable bandgaps, long carrier lifetimes and fairly small effective masses, amongst other factors.[9,10] However, the moisture sensitivity and toxicity of lead may limit wider commercialisation of such materials.[11] These issues represent the biggest challenges in the field to date and are topics of great current interest.

In the search for lead-free alternatives, Bi^{3+} based compounds have recently attracted attention. Examples include the preparation of low-dimensional compounds such as $A_3Bi_2I_9$ (A = K^+, Cs^+, Rb^+, $[NH_4]^+$ and $[CH_3NH_3]^+$), as well as the investigation of (hybrid) double perovskites.[12–14] In particular, the study of double perovskites in which the 3D perovskite-motif is maintained seems to be a promising avenue. In such materials, the perovskite formula is essentially doubled and the divalent metal cations, *e.g.* Pb^{2+} cations, are replaced by a monovalent and a trivalent cation, *e.g.* Na^+ and Bi^{3+}. The inorganic phases of general formula $A_2B^IB^{III}X_6$, with A = Cs^+, B^I = Na^+, Ag^+, B^{III} = Bi^{3+} and X = Cl^-, Br^-, have been investigated since the 70s,[15–18] initially in the context of ferroelectrics. Recently, we reported the synthesis and properties of the first inorganic–organic *hybrid* double perovskite $(MA)_2KBiCl_6$ ($MA^+ = [CH_3NH_3]^+$).[19] At this point no double perovskite iodides have been reported, although there has been a first principles computational study on $(MA)_2TlBiI_6$.[20] The application of these systems as photovoltaic absorbers is limited due to unfavourable electronic properties, originating from the ionic character of Cl^- and Br^- bonds. For example, the bandgap of our recent $(MA)_2KBiCl_6$ is approximately 3 eV. However, it would be expected that the use of Pearson-softer anions and cations, such as Br^- or I^- with, say, Tl^+ or Ag^+ as B^I may lead to enhanced optoelectronic properties. Motivated by our previous findings, we now report an in-depth computational screening study on lead-free hybrid double perovskites as potential photovoltaic absorbers. In particular, we apply density function theory (DFT) calculations to study the series of hybrid double perovskites $(MA)_2B^IB^{III}X_6$ with B^I = K^+, Tl^+, Ag^+, Cu^+, B^{III} = Bi^{3+}, and X = Cl^-, Br^- and I^- (Fig. 1). Additionally, we describe the synthesis and optical properties of a new double hybrid perovskite, $(MA)_2TlBiBr_6$, which is isoelectronic with $MAPbBr_3$ and has a much narrower bandgap than $(MA)_2KBiCl_6$.

Department of Materials Science and Metallurgy, University of Cambridge, 27 Charles Babbage Road, Cambridge CB3 0FS, UK. E-mail: pdb1000@cam.ac.uk; akc30@cam.ac.uk

† Electronic supplementary information (ESI) available: Calculated structural, electronic and mechanical information, X-ray structure for $(MA)_2TlBiBr_6$ nanoindentation and DSC details. CCDC 1485581. For ESI and crystallographic data in CIF or other electronic format see DOI: 10.1039/c6ta05817e

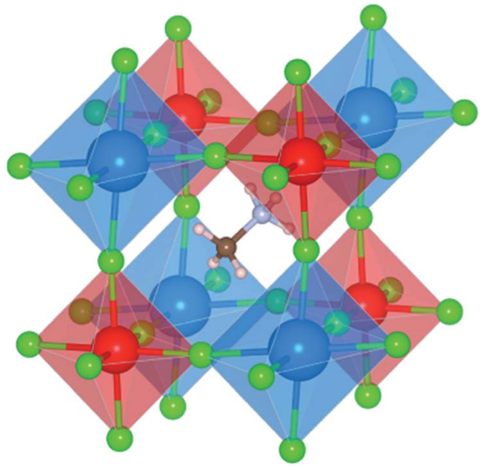

Fig. 1 Crystal structure of (MA)$_2$B^{I}B^{III}X$_6$. Blue: B^I, red: B^{III}, pink: H, brown: C, grey: N, green: X. B^{I}X$_6$ and B^{III}X$_6$ octahedra are shown in blue and red, respectively. Structure was produced using the VESTA program.[21]

The DFT calculations were performed using the *Vienna Ab Initio Simulation Package* (VASP).[22,23] Details of the methodology, including pseudopotentials, exchange–correlation functional, *k*-point mesh, kinetic energy cut-off and convergence criteria, are given in the ESI.† Importantly for hybrid materials containing heavy elements, van der Waals forces and spin–orbit coupling (SOC) were included. Since (MA)$_2$KBiCl$_6$ is observed to crystallise in the $R\bar{3}m$ space group, the same symmetry was applied to the calculated structures both initially and during geometry optimisation (see ESI page 2†). This allows for direct comparison with the experiments and enables trends in behaviour to be studied. In addition to the group of 12 double hybrid perovskites listed above, a further 3 structures of the form MAPbX$_3$ with B^I = B^{III} = Pb were computed as a reference set. Following equilibration, the atomic and electronic structures of each perovskite were analysed with particular focus on the effect of the ionic radius on the band gap and the mechanical stability of the structures.

The computed lattice constants (referred to hexagonal axes), equilibrium volumes and c/a ratios of the 15 structures as a function of the X anion radii are given in Table S1 and displayed in Fig. S1.† It is seen that the first two quantities increase with increasing anion radius, as expected ($r_{\mathrm{Cl}} = 180$ pm, $r_{\mathrm{Br}} = 196$ pm and $r_{\mathrm{I}} = 220$ pm).[24] The almost constant variation in c/a ratio indicates that the lattice expansion is approximately isotropic. The various interatomic distances (*e.g.* B^I–X, N⋯X and C⋯X) as a function of the X radii are given in Table S2 and Fig. S2,† and again show an increasing trend with anion radius. Furthermore, as the effective radius of the B^I cation increases the bond distances also generally increase for each halide ($r_{\mathrm{Cu}} = 77$ pm, $r_{\mathrm{Ag}} = 115$ pm, $r_{\mathrm{K}} = 138$ pm and $r_{\mathrm{Tl}} = 150$ pm).[24] Each of these results is consistent with expectations based on the relative sizes of the ions. Hydrogen bonding contributes to the stability of each structure and it can be seen from Fig. S2† that X⋯H bond distances, for example, increase as the X anion becomes less electronegative, indicating a weakening of the H-bonds. The various bond angles (*e.g.* B^I–X–B^{III}, X–B^{III}–X and C–H⋯X) as a function of the X radii are given in Table S3 and Fig. S3† and do not show a strong variation with anion radius. In addition, the angles do not deviate much from those expected for the ideal geometry, *e.g.* 180° for B^I–X–B^{III}, indicating that tilting of the B^{I}X$_6$ and B^{III}X$_6$ octahedra is relatively small. For example, Pb–I–Pb is 177.5° in MAPbI$_3$ whereas in the low temperature, orthorhombic MAPbI$_3$, which is known to exhibit significant tilting, the equivalent computed angle is 145°.[25]

Fig. 2 and Table S4† give the calculated band gaps of the 15 structures as a function of the X anion radii, where it is seen that the gap decreases by up to 1 eV as the X radii increase. Furthermore, the B^I cation can significantly lower the band gap for a given halide. In all cases the largest gap is found when B^I = K (*e.g.* 3.02 eV for (MA)$_2$KBiCl$_6$) and the smallest gap when B^I = Cu (*e.g.* 0.28 eV for (MA)$_2$CuBiI$_6$). The calculated gaps for the MAPbX$_3$ reference structures are close to previous calculations for their cubic counterparts.[26] Similar trends in band gaps have been reported for the corresponding inorganic Cs compounds: Cs$_2$B^{I}BiCl$_6$ > Cs$_2$B^{I}BiBr$_6$ > Cs$_2$B^{I}BiI$_6$ and Cs$_2$CuBiX$_6$ < Cs$_2$AgBiX$_6$.[16] Fig. S4† shows that the band gap systematically decreases as B^I–X–B^{III} approaches 180°, which is in agreement with previous calculations on single perovskites, showing that smaller octahedral tilts result in reduced band gaps.[27]

To understand the origin of these effects, the projected densities of states (PDOS) were calculated and are shown in Fig. S5–S7,† where attention is paid to the band edges. First, it is seen that the MA$^+$ cation does not contribute to states at the band edges, in agreement with previous studies on MAPbI$_3$.[28] It is interesting to note that if the MA$^+$ cation is replaced with Cs$^+$ in the double perovskites Cs$_2$AgBiCl$_6$ and Cs$_2$AgBiBr$_6$, the Cs$^+$ cation also does not contribute to states near the band edges.[17] Second, X-p states make a large contribution at both the valence band maximum (VBM) and the conduction band minimum (CBM). This indicates that choosing the appropriate halogen, specifically iodine, is important for obtaining a small band gap, semiconducting material. Similarly, appropriate choice of the B^I cation is essential because using K$^+$, for example, which is

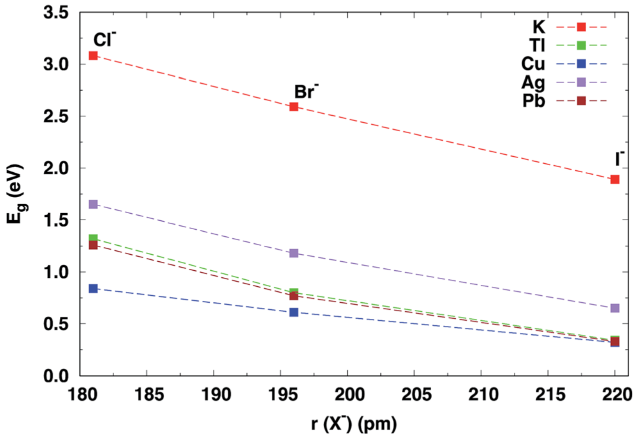

Fig. 2 Computed band gaps of (MA)$_2$B^{I}BiX$_6$ where B^I = K, Tl, Cu and Ag as a function of X anion radius, including the MAPbX$_3$ reference structures.

strongly ionic, leads to an undesirably large band gap. This is because only X-p, Bi-6s and Bi-6p orbitals contribute to the band edge states (Fig. S5†). However, using Tl^+, Tl-6s and Tl-6p orbitals also make a contribution, which reduces the band gap significantly (Fig. S5†). This is similar to the situation in $MAPbX_3$ where Pb-6s and Pb-6p orbitals are present near the band edges (Fig. S7†). Incorporating Cu^+ onto the B^I site further reduces the band gap due to the presence of Cu-3d orbitals near the VBM (Fig. S6†).

The electronic band structures of the 15 perovskites are collected in Fig. S8.† The band shapes near the band edges, which determine the carrier effective masses, fluctuate more with respect to the X anion than with respect to the B^I cation. $B^I = K^+$ produces the flattest bands while $B^I = Tl^+$ or Pb^+ gives the most curved bands. Although all the structures contain the MA^+ cation, their band gaps and carrier effective masses differ widely. The locations of the VBM and CBM within the Brillouin zone depend mostly on the B^I cation, except for K^+, and are largely independent of the X anion, as shown in Table S5.† When $B^I = Tl^+$ the band gap is direct, but when $B^I = Cu^+$ or Ag^+ it is indirect due to the orbital interactions introduced by the different elements (see Fig. S13 and notes in the ESI†). It is seen that the band structures of $(MA)_2CuBiX_6$ and $(MA)_2AgBiX_6$ are quite similar due to their similar electronic configurations. Furthermore, because $(MA)_2TlBiX_6$ and $MAPbX_3$ are isoelectronic, their band structures are also very similar, as illustrated in Fig. 3 below for $X = Br^-$.

The mechanical stability of the hybrid double perovskites considered here is important if they are to be considered for real world device applications. Tables S6 and S7† give the calculated single crystal stiffness constants (C_{ij}) of the 15 structures and the corresponding polycrystalline values of Young's modulus (E), bulk modulus (B), shear modulus (G) and Poisson's ratio (ν). The stiffness constants are calculated from the stress–strain relationship by applying two types of strains to the unit cells,[29] e_1 and $e_3 + e_4$. $(MA)_2AgBiCl_6$, $(MA)_2AgBiBr_6$, $(MA)_2CuBiCl_6$ and $(MA)_2CuBiBr_6$ are found to be unstable when ±1% strains are applied due a rotation of the MA^+ cation making the stress–strain relationship nonlinear. Therefore, the stiffness constants are obtained using only ±0.5% strains, but even then the negative eigenvalues of the stiffness matrix indicate that $(MA)_2CuBiCl_6$ and $(MA)_2CuBiBr_6$ remain unstable.[30]

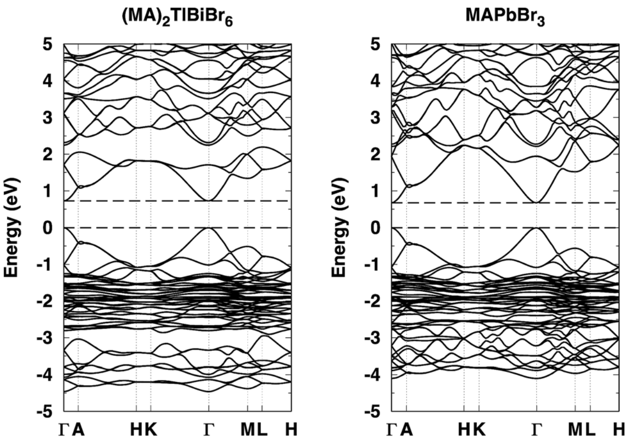

Fig. 3 Computed electronic band structures of $(MA)_2TlBiBr_6$ and $MAPbBr_3$.

Fig. 4 shows the polycrystalline elastic constants as a function of X anion radius, demonstrating that E, B and G decrease with increasing anion radius, in agreement with the trend observed from nano-indentation experiments on tetragonal $MAPbX_3$.[31] This can be explained by a decrease in the strength of the X⋯H and B–X bonds as the anion radius increases. However, it is found that the Young's moduli of the rhombohedral form of $MAPbX_3$ considered here are larger than the experimental results, probably because of the imposed symmetry constraints. The Poisson's ratio is largely independent of X anion radius. The directional dependencies of the single crystal Young's moduli of $(MA)_2KBiX_6$, $(MA)_2TlBiX_6$, $(MA)_2AgBiX_6$ and $MAPbX_3$ are shown in Fig. S9–S12 and discussed in the ESI.†

A comparison between the Young's moduli of $MAPbX_3$ and $(MA)_2TlBiX_6$ shows that the isoelectronic substitution of Pb by Bi + Tl makes the structure less stiff, which is similar to findings in our previous studies on zeolitic imidazolate frameworks, when Zn is replaced by Li + B.[32] This can be explained by comparing the bond strength of Pb–X in $MAPbX_3$ with Bi–X and Tl–X in $(MA)_2TlBiX_6$. Assuming that bond strength and bond distance (d) are directly correlated, Fig. S2† shows that $d_{Tl-X} > d_{Pb-X} > d_{Bi-X}$, which indicates that Bi–X is stronger than Pb–X and Tl–X. When applying strains, the weaker Tl–X bond results in a more flexible $(MA)_2TlBiX_6$ structure compared with $MAPbX_3$.

Motivated by the results from our DFT calculations, we have attempted to synthesise all the predicted phases using hydrothermal, solvent evaporation and solid state sintering methods. Despite the success with our previously reported $(MA)_2KBiCl_6$, we have only managed to obtain one other hybrid double

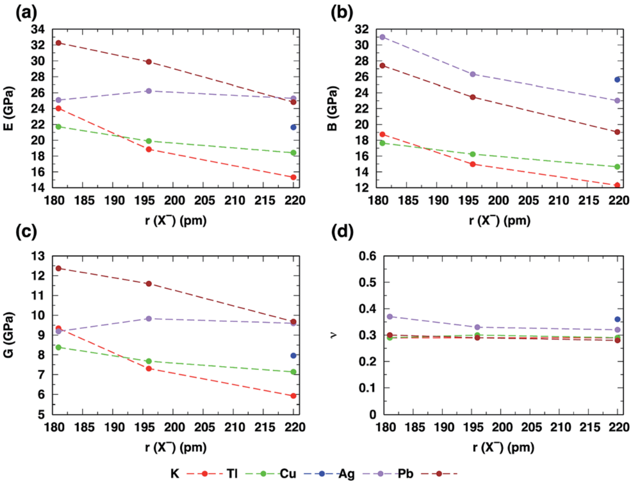

Fig. 4 Polycrystalline values of (a) Young's modulus E, (b) bulk modulus B, (c) shear modulus G and (d) Poisson's ratio of $(MA)_2B^IBiX_6$ where B^I = K, Tl, Cu and Ag as a function of the X anion radius.

perovskite. $(MA)_2TlBiBr_6$ was synthesized by the hydrothermal method at 150 °C using 3 mmol MABr, 1.5 mmol $(CH_3COO)Tl$, and 1.5 mmol $BiBr_3$ in 1 ml HBr. The product was a mixture containing significant quantities of yellowish $(MA)_2Bi_3Br_9$. The double perovskite crystals are dark red in color, and can be easily separated manually from the mixture for further analysis. For the other compositions, although the appropriate starting stoichiometry was applied, the products were either $(MA)_3BiX_6$ ($X = Cl^-$) or $(MA)_3Bi_2X_9$ ($X = Br^-, I^-$). This could be because there is either an issue with kinetics during synthesis of the double perovskites or perhaps $(MA)_3Bi_2X_9$ is a thermodynamically favoured phase.

$(MA)_2TlBiBr_6$, crystallises in space group $Fm\bar{3}m$ (a = 11.762(2) Å), with Tl^+ and Bi^{3+}, isoelectronic with Pb^{2+}, occupy alternating octahedral sites. The MA^+ cations are disordered, and the corresponding size of the electron density is ~2.25 Å, similar to the size of MA^+ (2.17 Å). Based on the size and the relatively isotropic electron density core, a rotational rather than translational motion of the organic cations in the cavity is suggested. A model wherein MA^+ is observed as an octahedron in the cavity with a restrained C–N length of 1.4 Å was applied, as shown in Fig. S14.† A similar approach was used by Weller *et al.* in their variable temperature neutron studies on $MAPbI_3$.[33] In this model, C and N occupy symmetry equivalent sites, each with a partial occupancy of 1/6. Structural refinement without MA^+ gives $R_{obs} = 6.31$, with positive and negative residue electron densities of −2.65 and 2.29, respectively, while using this model R_{obs} drops to 4.24 and the residues reduce to −1.71 and 1.73. A list of inorganic atomic coordinates is given in Table S8.† The bond length of Bi–Br is 2.794(4) Å and that of Tl–Br is 3.087(4) Å, which are comparable with the calculated bond lengths of 2.854 Å and 3.145 Å, respectively, from our DFT calculations. The Pb–Br bond length is 2.965 Å in the previously reported cubic $MAPbBr_3$.[5]

Differential scanning calorimetry (DSC) was conducted on $(MA)_2TlBiBr_6$ using a DSC instrument Q2000 from 25 °C to −150 °C under liquid nitrogen flow of 100 ml min^{-1}, with a ramping rate of 10 °C min^{-1}. Two possible phase transitions are present, at approximately −10 °C and −25 °C (Fig. S15†). Based on our previous report on the $(MA)_2KBiCl_6$ analogue,[19] it can reasonably be predicted that one of the low temperature phases would have rhombohedral symmetry. Low temperature single crystal X-ray diffraction, even at −20 °C, indicate heavy twinning, confirming that a phase transition takes place but making it very difficult to determine the structure. Further studies on the phase transitions will be carried out in the future using resonant ultrasound spectroscopy and variable temperature powder X-ray diffraction.

Optical measurements were carried out on $(MA)_2TlBiBr_6$ using a PerkinElmer Lambda 750 UV-Visible spectrometer in the reflectance mode with a 2 nm slit width. The scan interval was 1 nm and the scan range was between 350 and 1000 nm. By assuming a direct band gap as suggested in the DFT calculation, a Tauc plot is constructed which estimates the optical band gap to be ~2.16 eV (Fig. 5). This is comparable with that of $MAPbBr_3$ (2.2–2.35 eV)[5,34] and is further consistent with the DFT calculations where the band structures of $(MA)_2TlBiX_6$ are predicted to be similar to the corresponding Pb analogues. Based on the structural and electronic analysis, the $(MA)_2TlBiX_6$ systems provide interesting alternatives to lead-containing perovskites, while noting that thallium itself is also toxic. The DFT calculations, which include SOC, underestimate the band gap for $(MA)_2TlBiBr_6$ (0.72 eV), as was the case for the previously reported $MAPbI_3$, with 0.60 eV from DFT with SOC compared to 1.55 eV from experiments.[35]

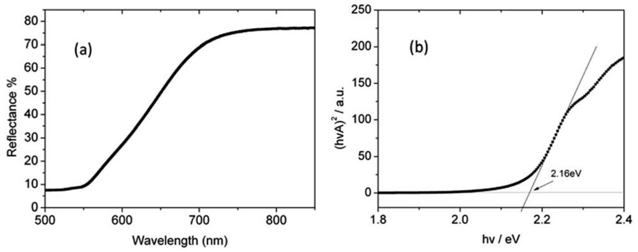

Fig. 5 (a) Reflectance spectrum for $(MA)_2TlBiBr_6$, and (b) corresponding Tauc plot assuming a direct band gap.

Nanoindentation experiments were performed on $(MA)_2TlBiX_6$ single crystals at room temperature, following the methods described previously.[31] A Young's modulus of 12.8 ± 1.9 GPa and hardness of 0.56 ± 0.10 GPa were observed with the indenter tip normal to the (111) facets in a cubic structure (see Fig. S16†). The experimental Young's modulus is consistent with the computational result (11.98 GPa) along the equivalent direction in the rhombohedral structure (see Fig. S10 and Table S7†).

Conclusions

In conclusion, we have used DFT calculations to predict that some of the double perovskites of general formula $(MA)_2B^IBiX_6$ offer interesting alternatives to their lead-containing analogues, $MAPbX_3$, for photovoltaic applications, with band gaps and electronic structures that are similar to the lead-containing phases. Furthermore, we have synthesised a new double perovskite, $(MA)_2TlBiBr_6$, that is isoelectronic with $MAPbBr_3$ and has strikingly similar properties. Further reactions are being undertaken with the aim of obtaining additional phases in the hybrid double perovskite family.

Acknowledgements

Z. Deng and S. Sun would like to thank the Cambridge Overseas Trust and the China Scholarship Council. F. Wei is a holder of an A*STAR international fellowship granted by the Agency for Science, Technology and Research, Singapore. The calculations were performed at the Cambridge HPCS and the UK National Supercomputing Service, ARCHER. Access to the latter was obtained *via* the UKCP consortium and funded by EPSRC under Grant No. EP/K014560/1. G. Kieslich and A. K. Cheetham gratefully thank the Ras Al Kaihmah Center for Advanced Materials for financial support.

Notes and references

1 M. D. McGehee, *Nat. Mater.*, 2014, **13**, 845–846.

2 A. Kojima, K. Teshima, Y. Shirai and T. Miyasaka, *J. Am. Chem. Soc.*, 2009, **131**, 6050–6051.

3 M. M. Lee, J. Teuscher, T. Miyasaka, T. N. Murakami and H. J. Snaith, *Science*, 2012, **338**, 643–647.

4 J. Burschka, N. Pellet, S.-J. Moon, R. Humphry-Baker, P. Gao, M. K. Nazeeruddin and M. Grätzel, *Nature*, 2013, **499**, 316–319.

5 T. Baikie, N. S. Barrow, Y. Fang, P. J. Keenan, P. R. Slater, R. O. Piltz, M. Gutmann, S. G. Mhaisalkar and T. J. White, *J. Mater. Chem. A*, 2015, **3**, 9298–9307.

6 A. Jaffe, Y. Lin, C. M. Beavers, J. Voss, W. L. Mao and H. I. Karunadasa, *ACS Cent. Sci.*, 2016, **2**, 201–209.

7 J. M. Frost and A. Walsh, *Acc. Chem. Res.*, 2016, **49**, 528–535.

8 A. L. Montero-Alejo, E. Menéndez-Proupin, D. Hidalgo-Rojas, P. Palacios, P. Wahnón and J. C. Conesa, *J. Phys. Chem. C*, 2016, **120**, 7976–7986.

9 T. M. Brenner, D. A. Egger, A. M. Rappe, L. Kronik, G. Hodes and D. Cahen, *J. Phys. Chem. Lett.*, 2015, **6**, 4754–4757.

10 L. M. Pazos-Outon, M. Szumilo, R. Lamboll, J. M. Richter, M. Crespo-Quesada, M. Abdi-Jalebi, H. J. Beeson, M. Vruini, M. Alsari, H. J. Snaith, B. Ehrler, R. H. Friend and F. Deschler, *Science*, 2016, **351**, 1430–1433.

11 S. Yang, Y. Wang, P. Liu, Y.-B. Cheng, H. J. Zhao and H. G. Yang, *Nature Energy*, 2016, **1**, 15016.

12 A. J. Lehner, D. H. Fabini, H. A. Evans, C.-A. Hébert, S. R. Smock, J. Hu, H. Wang, J. W. Zwanziger, M. L. Chabinyc and R. Seshadri, *Chem. Mater.*, 2015, **27**, 7137–7148.

13 B. Chabot and E. Parthé, *Acta Crystallogr., Sect. B: Struct. Crystallogr. Cryst. Chem.*, 1978, **34**, 645–648.

14 S. Sun, S. Tominaka, J.-H. Lee, F. Xie, P. D. Bristowe and A. K. Cheetham, *APL Mater.*, 2016, **4**, 031101.

15 A. H. Slavney, T. Hu, A. M. Lindenberg and H. I. Karunadasa, *J. Am. Chem. Soc.*, 2016, **138**, 2138–2141.

16 G. Volonakis, M. R. Filip, A. A. Haghighirad, N. Sakai, B. Wenger, H. J. Snaith and F. Giustino, *J. Phys. Chem. Lett.*, 2016, **7**, 1254–1259.

17 E. T. McClure, M. R. Ball, W. Windl and P. M. Woodward, *Chem. Mater.*, 2016, **28**, 1348–1354.

18 L. R. Morss, M. Siegal, L. Stenger and N. Edelstein, *Inorg. Chem.*, 1970, **9**, 1771–1775.

19 F. Wei, Z. Deng, S. Sun, F. Xie, G. Kieslich, D. M. Evans, M. A. Carpenter, P. D. Bristowe and A. K. Cheetham, *Mater. Horiz.*, 2016, **3**, 328–332.

20 G. Giorgi and K. Yamashita, *Chem. Lett.*, 2015, **44**, 826–828.

21 K. Momma and F. Izumi, *J. Appl. Crystallogr.*, 2011, **44**, 1272–1276.

22 G. Kresse, *J. Non-Cryst. Solids*, 1995, **192–193**, 222–229.

23 G. Kresse and J. Furthmüller, *Comput. Mater. Sci.*, 1996, **6**, 15–50.

24 R. D. Shannon, *Acta Crystallogr., Sect. A: Found. Crystallogr.*, 1976, **32**, 751–767.

25 J.-H. Lee, N. C. Bristowe, P. D. Bristowe and A. K. Cheetham, *Chem. Commun.*, 2015, **51**, 6434–6437.

26 J. Even, L. Pedesseau, J.-M. Jancu and C. Katan, *J. Phys. Chem. Lett.*, 2013, **4**, 2999–3005.

27 J.-H. Lee, N. C. Bristowe, J. H. Lee, S.-H. Lee, P. D. Bristowe, A. K. Cheetham and H. M. Jang, *Chem. Mater.*, 2016, **28**, 4259–4266.

28 A. Filippetti and A. Mattoni, *Phys. Rev. B: Condens. Matter Mater. Phys.*, 2014, **89**, 125203.

29 Y. Le Page and P. Saxe, *Phys. Rev. B: Condens. Matter Mater. Phys.*, 2002, **65**, 104104.

30 F. Mouhat and F.-X. Coudert, *Phys. Rev. B: Condens. Matter Mater. Phys.*, 2014, **90**, 224104.

31 S. Sun, Y. Fang, G. Kieslich, T. J. White and A. K. Cheetham, *J. Mater. Chem. A*, 2015, **3**, 18450–18455.

32 T. D. Bennett, J.-C. Tan, S. A. Moggach, R. Galvelis, C. Mellot-Draznieks, B. A. Reisner, A. Thirumurugan, D. R. Allan and A. K. Cheetham, *Chem.–Eur. J.*, 2010, **16**, 10684–10690.

33 M. T. Weller, O. J. Weber, P. F. Henry, M. Di Pumpo and T. C. Hansen, *Chem. Commun.*, 2015, **51**, 3–6.

34 H. Bin Kim, I. Im, Y. Yoon, S. Do Sung, E. Kim, J. Kim and W. I. Lee, *J. Mater. Chem. A*, 2015, **3**, 9264–9270.

35 P. Umari, E. Mosconi and F. De Angelis, *Sci. Rep.*, 2014, **4**, 4467.